Electronic Supplementary Material (ESI) for Chemical Communications.

Supplementary Information

Platinum-like HER Onset in GNR/MoS_2 Quantum Dots Heterostructure Through Curvature-dependent Electron Density Reconfiguration

Aruna Narayanan Nair, [a] Mohamed F Sanad, [b] Venkata S. N. Chava, [a] and Sreeprasad T. Sreenivasan [*a]

a Department of Chemistry and Biochemistry, The University of Texas at El Paso, El Paso, Texas 79968, United States. Email: sreenivasan@utep.edu

b Department of Environmental Sciences and Engineering, The University of Texas at El Paso, El Paso, Texas 79968, United States

Table of Contents

1.1 Oxidative unzipping of multiwalled carbon nanotubes using $KMnO_4$

MWCNTs were used as received from Millipore sigma. For unzipping process initially, the MWCNTs were suspended in concentrated sulfuric acid (H_2SO_4) for a period of 1–12 h and then treated them with 500 wt% potassium permanganate ($KMnO_4$). The reaction mixture was stirred at room temperature for 1 h and then heated to 55–70 ^oC for an additional 1 h. The mixture was agitated with a magnetic stirrer until all the $KMnO_4$ was consumed, as noted by the disappearance of the red tint upon diluting a sample of the reaction mixture with water. When all the $KMnO_4$ had been consumed, we quenched the reaction mixture by pouring over ice containing a small amount of hydrogen peroxide (H_2O_2). The solution was filtered over a polytetrafluoroethylene (PTFE) membrane, and the remaining solid was washed with water followed by ethanol.[1]

1.2 Oxidative unzipping of multiwalled carbon nanotubes using ammonium persulfate

The MWCNT (200 mg) was added to a 100 mL round-bottom flask containing a mixture of concentrated sulfuric acid (20 mL) and fuming sulfuric acid (20% free SO_3 basis, 20 mL). The suspension was stirred at room temperature for 5 min before adding $(NH_4)_2S_2O_8$ (5.0 g) and the flask was connected to a condenser. The reaction mixture was stirred at 80^oC for 24h and further quenched with ice. The product was then isolated by vacuum filtration, washed with water, ethanol, and acetone.[2]

1.3 Synthesis of MoS_2 QDs and GNR/MoS_2 heterostructure

A total of 5 mg of ammonium tetra thiomolybdate $(NH_4)_2MoS_4$ was dissolved in 30 mL of H_2O and sonicated up to 1 h. Then, 500 µL of hydrazine hydrate ($N_2H_4{\cdot}4H_2O$) was added and sonicated for another 1 h. The solution was transferred to a 40 mL autoclave and heated at 200 °C for 24 h. The resulting suspensions were centrifuged for 15 min at 10 000 rpm, and the supernatant solution with MoS_2 quantum dots is collected. The supernatant solution was purified by dialysis in water and lyophilized to get solid MoS_2 QDs for analysis. vdW heterostructure of GNRs and MoS_2 QDs (1:10 ratio) were fabricated via ultra-sonication method for 30 mins at room temperature.

1.4 Characterizations

The morphology of the GNR samples were studied using the S4800 scanning electron microscope. TEM images were obtained with FEI 300/80 Titan TEM and FEI Tecnai G (2) F30 S-Twin 300kV TEM. TEM samples were prepared by drop cast method over C-coated Cu grid. To remove agglomerates, the sample was sonicated to achieve a homogeneous dispersion. XPS measurements were performed using Kratos AXIS ULTRA X-ray Photoelectron Spectrometer. The Raman spectroscopy was conducted on a NT-MDT Raman spectrophotometer with 532 nm laser illumination. XRD measurements were performed on a p-XRD Empyrean 2 system. KPFM measurements were performed in two-pass amplitude mode (AM) using a Pt-coated conductive Si probe (FMG01/Pt, resonance frequency of 56 kHz).

1.5 Electrochemical measurements

The electrocatalytic performance was analyzed by cyclic voltammetry (CV), Linear sweep voltammetry (LSV), Electrochemical impedance spectroscopy (EIS) and chronoamperometric test by using an CHI660E CH instrument workstation. All the experiments were performed in a three-electrode configuration using platinum wire as a counter electrode, Ag/AgCl (3 M KCl) as a reference electrode, and a glassy carbon electrode having a 3 mm diameter as a working electrode. The electrolyte used was a 0.5 M aqueous H_2SO_4 solution. The potential against Ag/AgCl was converted into a potential against a reversible hydrogen electrode by using the following equation

$$E\ (RHE) = E\ (Ag/AgCl) + (0.197 + 0.059 * pH) \qquad (1)$$

1.6 Computational Details

Density Functional theory calculations were carried out using Cambridge sequential total energy package (CASTEP) in Material Studio software.[3] The generalized gradient approximation (GGA) of the Perdew−Burke−Ernzerh (PBE) functional was used to explain the exchange-correlation interactions. The GGA-PBE DFT method was adopted to consider the van der Waals (vdW) heterostructure. For geometric convergence, the thresholds for energy and force were set to 10^{-6} eV/atom and 0.02 eV/Å, respectively. Cutoff energy of 550 eV was selected for a plane wave basis.[4] The Isovalue of the electric field distribution is 0.0028. A 0.82-nm-diameter 2-layer MWCNT (8, 8) is fully and partly unzipped along the longitudinal axis into a flat GNR and partially unzipped curved GNR, respectively. The MWCNT (8, 8) is radially unzipped into curved and flat GNRs with lengths of 1.5 and 1.8 nm, respectively. Carboxylic acid groups were added to unzipped edges of the CNTs as obtained from the XPS results. MoS_2 Quantum dot structure was designed by creating a 3 × 3 × 1 2H-MoS_2 (002) supercell using crystal build property, from the bulk

2H-MoS_2.The D3H-MoS_6 units is the unit cell and the simplest representation of the MoS_2 quantum dots. For each structure, atomic positions were first relaxed to reach their equilibrium. The structural geometry optimization convergence thresholds for energy changes and displacement were set to be 1×10^{-6} Ha, 0.002 Å, and 2×10^{-4} Ha/Å. The SCF tolerance was set to 1.0×10^{-5} eV/atom and the wiping for the orbital occupancy was set to 0.05 Ha. For each elementary step in the HER, the Gibbs free energy was calculated using $\Delta G = \Delta E_{ad-H} + \Delta E_{ZPE} - T\Delta S_H$, where E_{ad-H} refers to the adsorption energy of H* (* denotes the uncertain ion state) on the catalytic site. ΔE_{ZPE} refers to the variance of zero-point energy, which can be found from vibration frequency calculations. T is temperature and ΔS_H is the half of S_H, which is a known thermodynamic feature for each adsorbate.

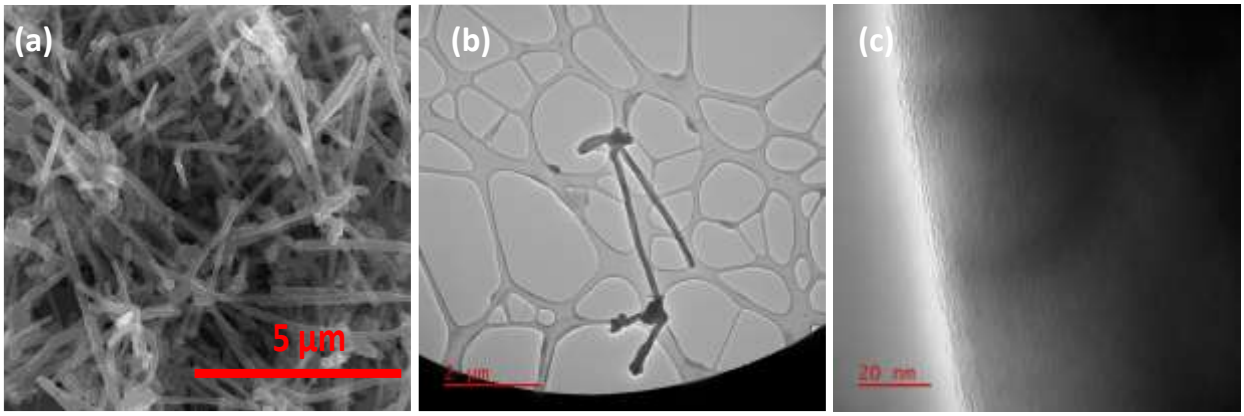

Fig. S1. (a) SEM image of pristine MWCNTS (b) Low resolution and (c) high resolution TEM images of MWCNT

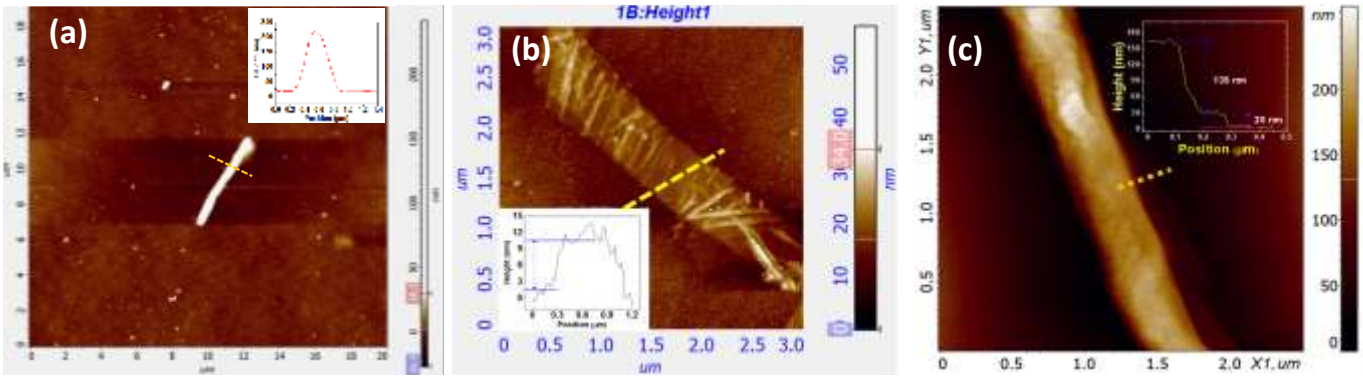

Fig. S2. AFM topography of (a) MWCNT, (b, c) of F-GNR and C-GNR, respectively. Insets are the height profiles corresponding to the lines marked in the topography images.

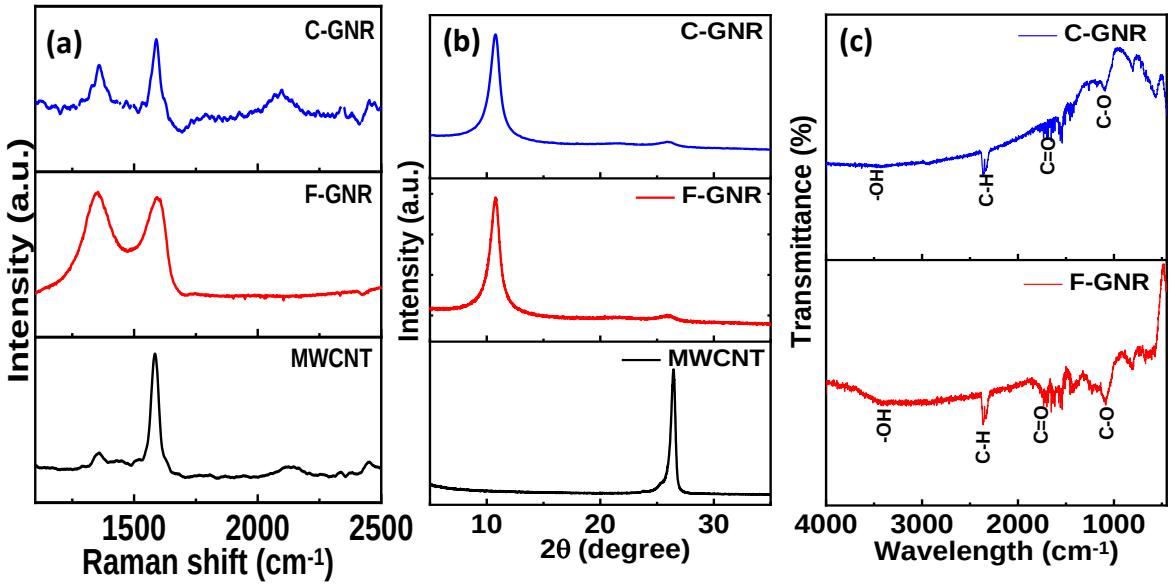

Fig. S3. (a) Raman spectrum of MWCNT, F-GNR and C-GNR (b) XRD spectrum of MWCNT, F-GNR and C-GNR and (c) FTIR of F-GNR and C-GNR

Sample	I_D/I_G
MWCNT	0.14
F-GNR	1.03
C-GNR	0.98

Table S1. I_D/I_G ratio from Raman spectrum for MWCNT, F-GNR and C-GNR

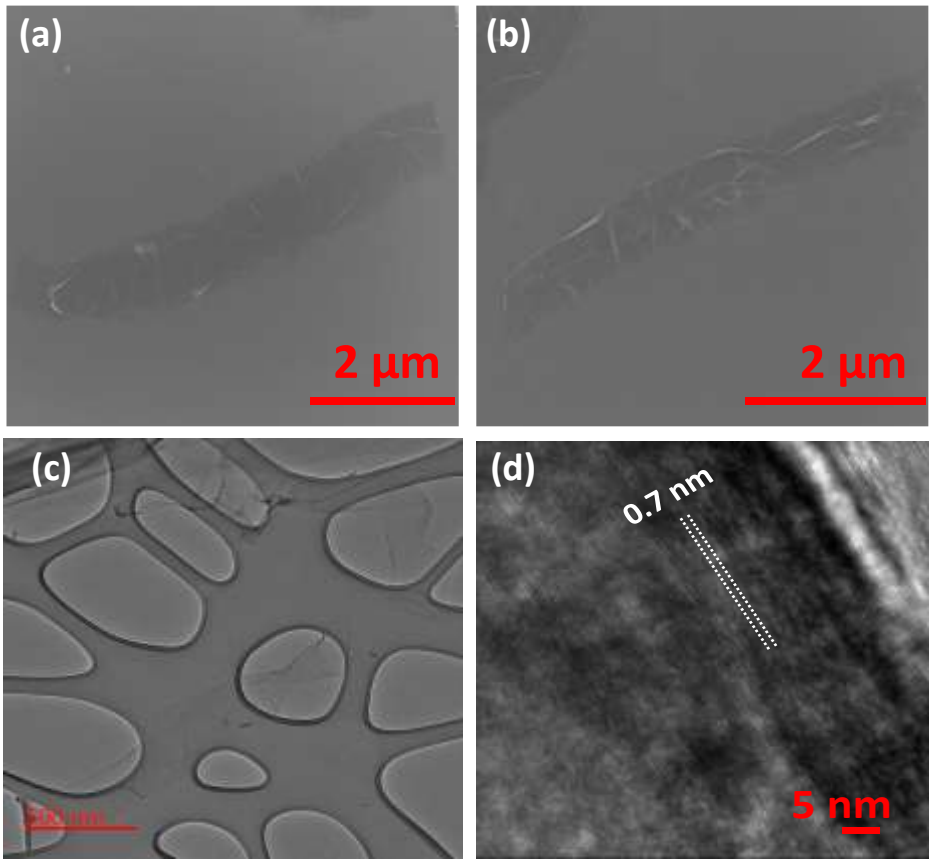

Fig. S4. (a, b) SEM images of F-GNRs (c) Low resolution TEM and (d) HRTEM images of F-GNR

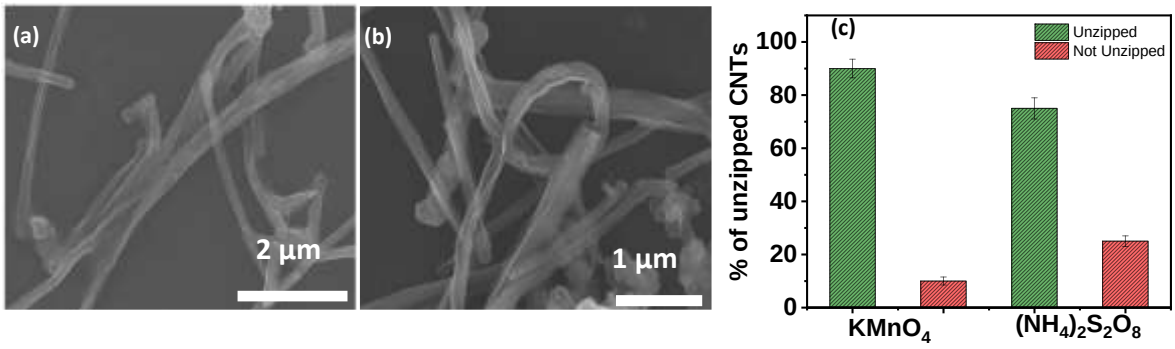

Fig. S5. (a, b) SEM images of C-GNR (c) degree of unzipping using the two oxidizing agents

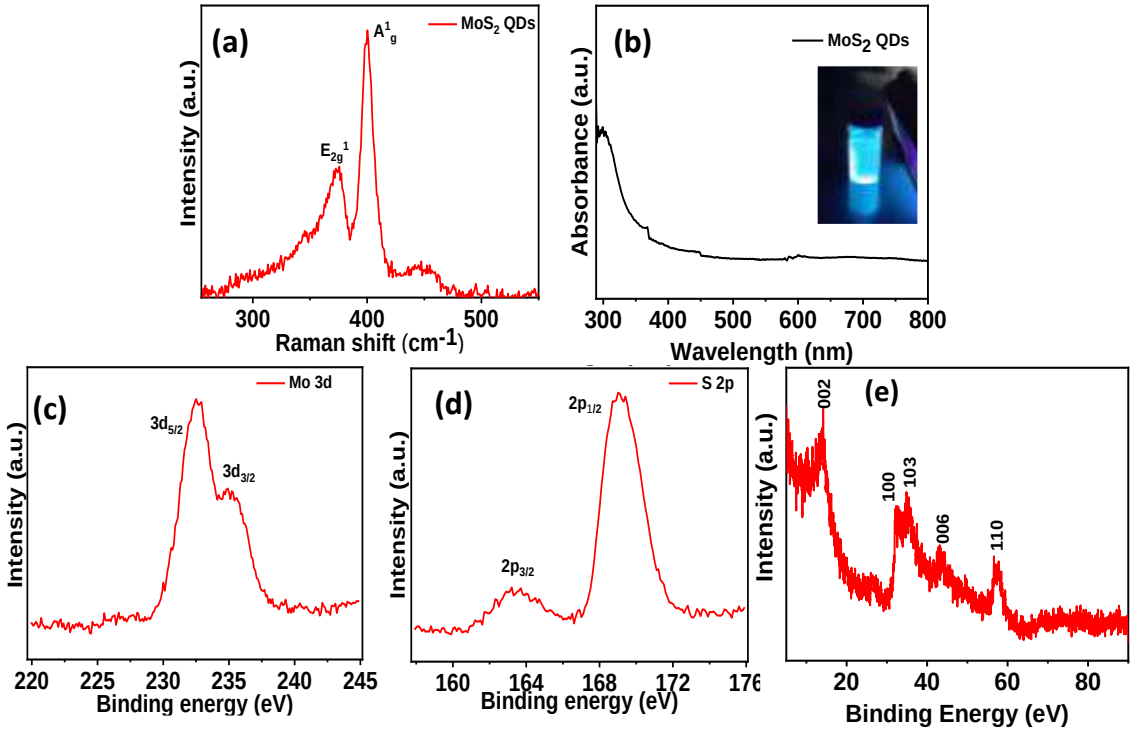

Fig. S6. (a) Raman spectrum of MoS_2 QDs (b) UV-Vis measurement (c, d) XPS high resolution spectrum of MoS_2 QDs (e) XRD of drop casted MoS_2 QDs solution on a glass slide

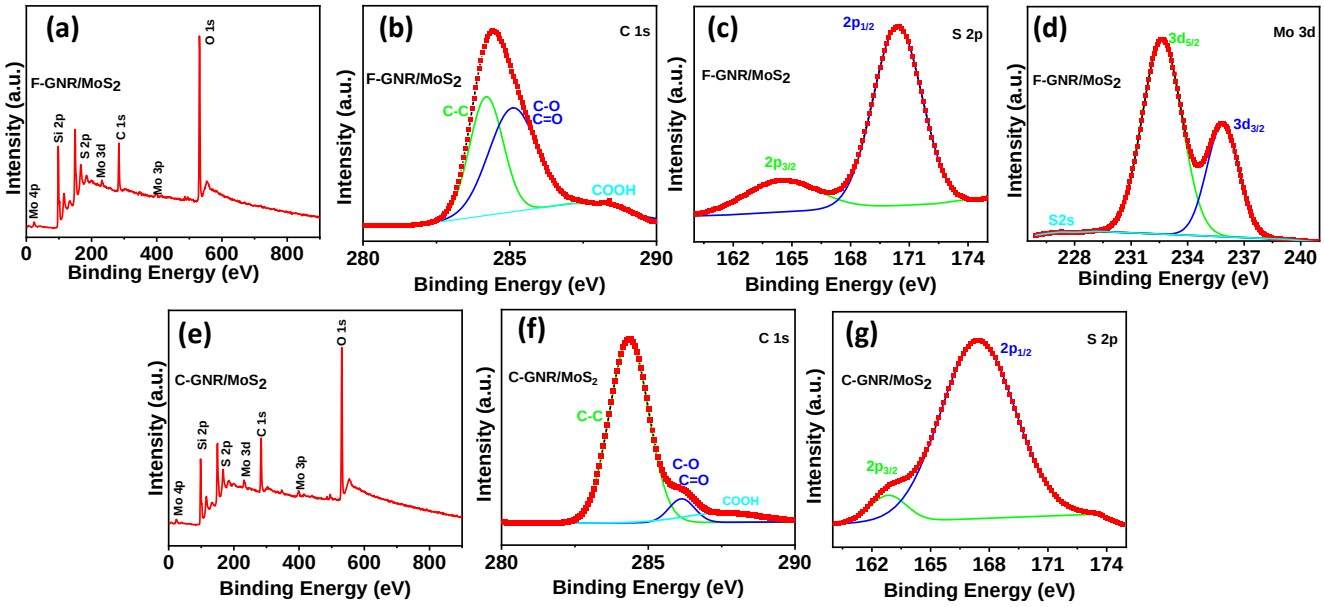

Fig. S7. XPS survey spectrum of (a) F-GNR/MoS_2, High resolution XPS spectra of F-GNR/MoS_2 (b) C 1s (c) S 2p (d) Mo 3d. XPS survey spectrum of (e) C-GNR/MoS_2 and High resolution XPS spectra of C-GNR/MoS_2 (f) C 1s (g) S 2p

The high-resolution Carbon XPS 1s spectra were deconvoluted and the peaks at 284 eV, 286 eV and 287 eV correspond to C-C, C–O and C=O, respectively. The shoulder peak at 289 eV is assigned to the carboxyl functional groups. The XPS of Sulfur species in the vdW heterostructures were also investigated as shown with major peaks located between binding energy of 160 and 176 eV corresponding to the S $2p_{3/2}$ and S $2p_{1/2}$ in MoS_2.

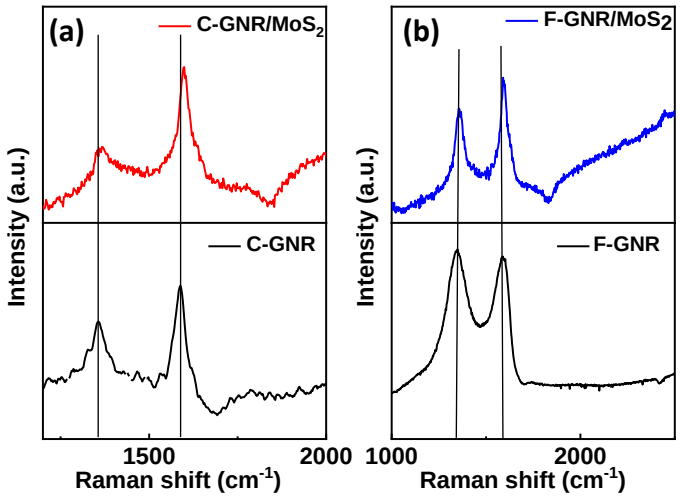

Fig. S8. Raman spectrum comparison

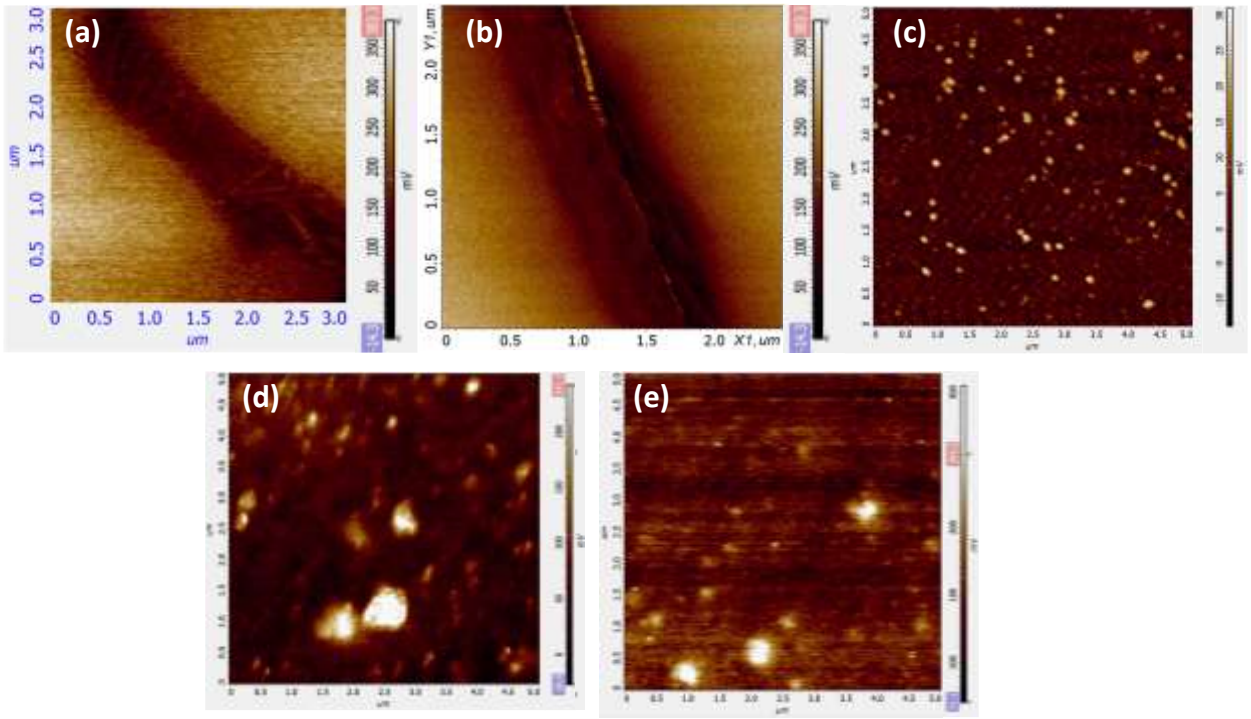

Fig. S9. KPFM surface potential maps of (a) F-GNR, (b) C-GNR and (c) MoS_2 QDs (d) C-GNR/MoS_2 and (e) F-GNR/MoS_2

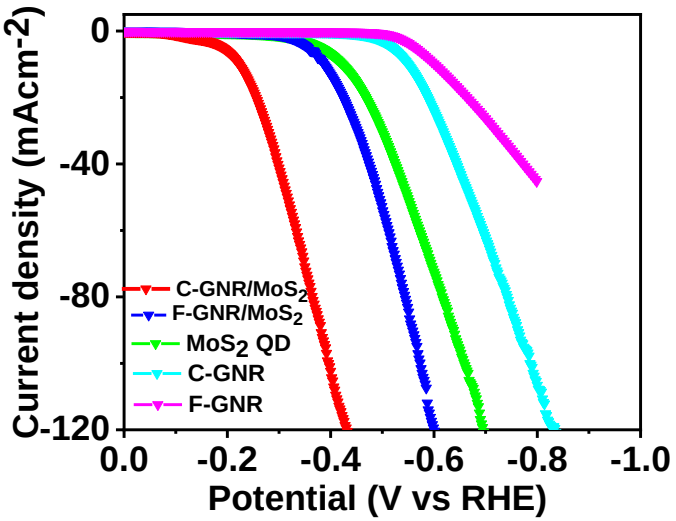

Fig. S10. Polarization curves for HER

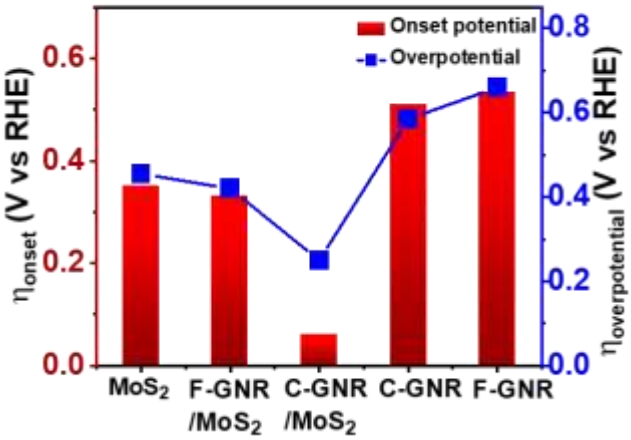

Fig. S11. Variation of onset potential and overpotential of MoS_2, C-GNR, F-GNR, C-GNR/MoS_2 and F-GNR/MoS_2

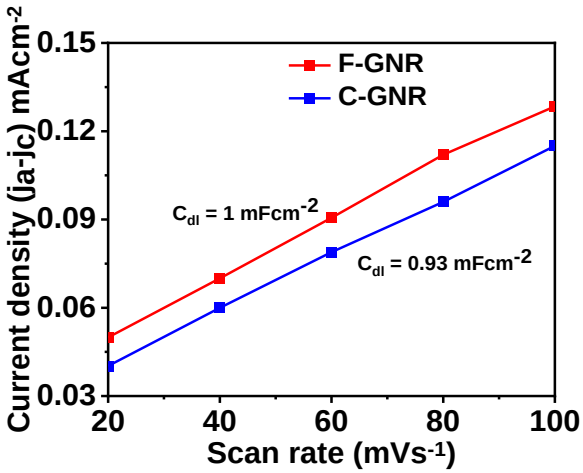

Fig. S12. Electrochemical surface area (ECSA) measurements of F-GNR and C-GNR

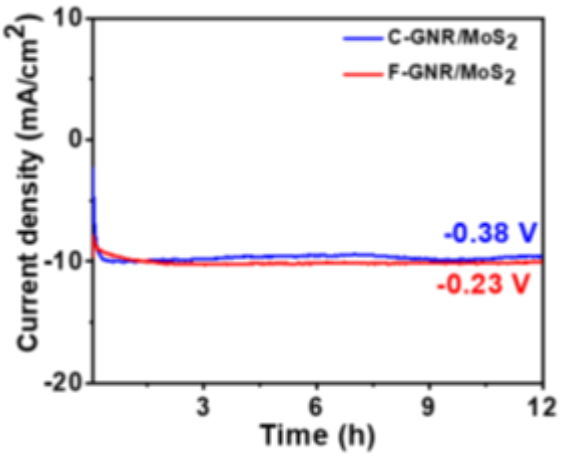

Fig. S13. Chronoamperometry measurements of C-GNR/MoS_2 and F-GNR/MoS_2

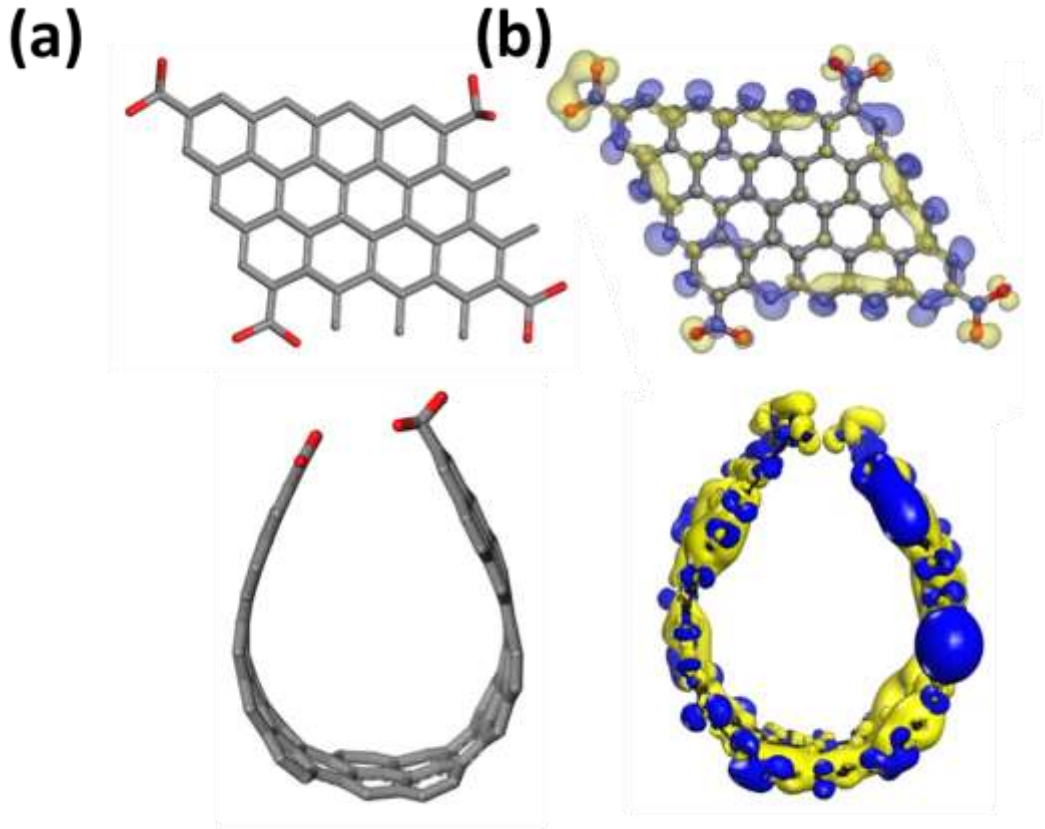

Fig. S14. DFT simulated structures (a) and electronic charge distribution of F-GNR and C-GNR

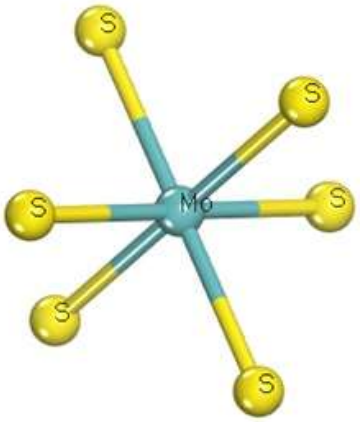

Fig. S15. Ball and stick representation of the MoS_2 QD structure

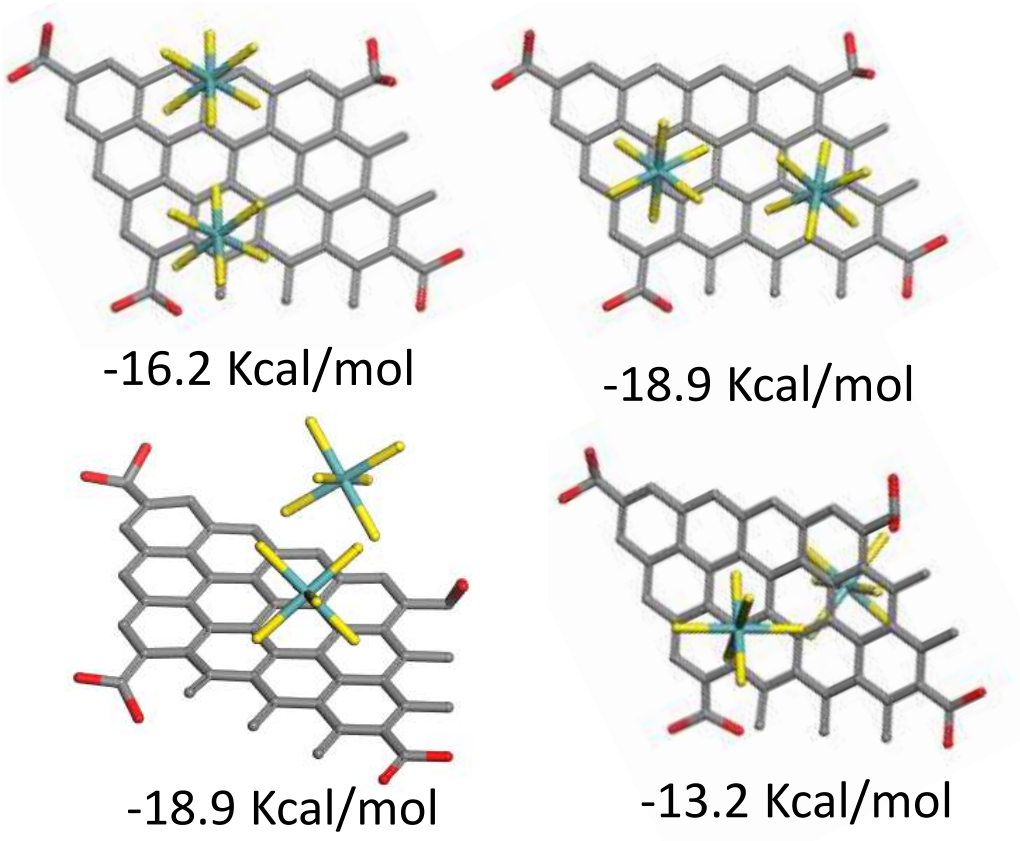

Fig. S16. Total energy of structures at different sites on F-GNR/ MoS_2. The lowest energy is the most possible and stable structure

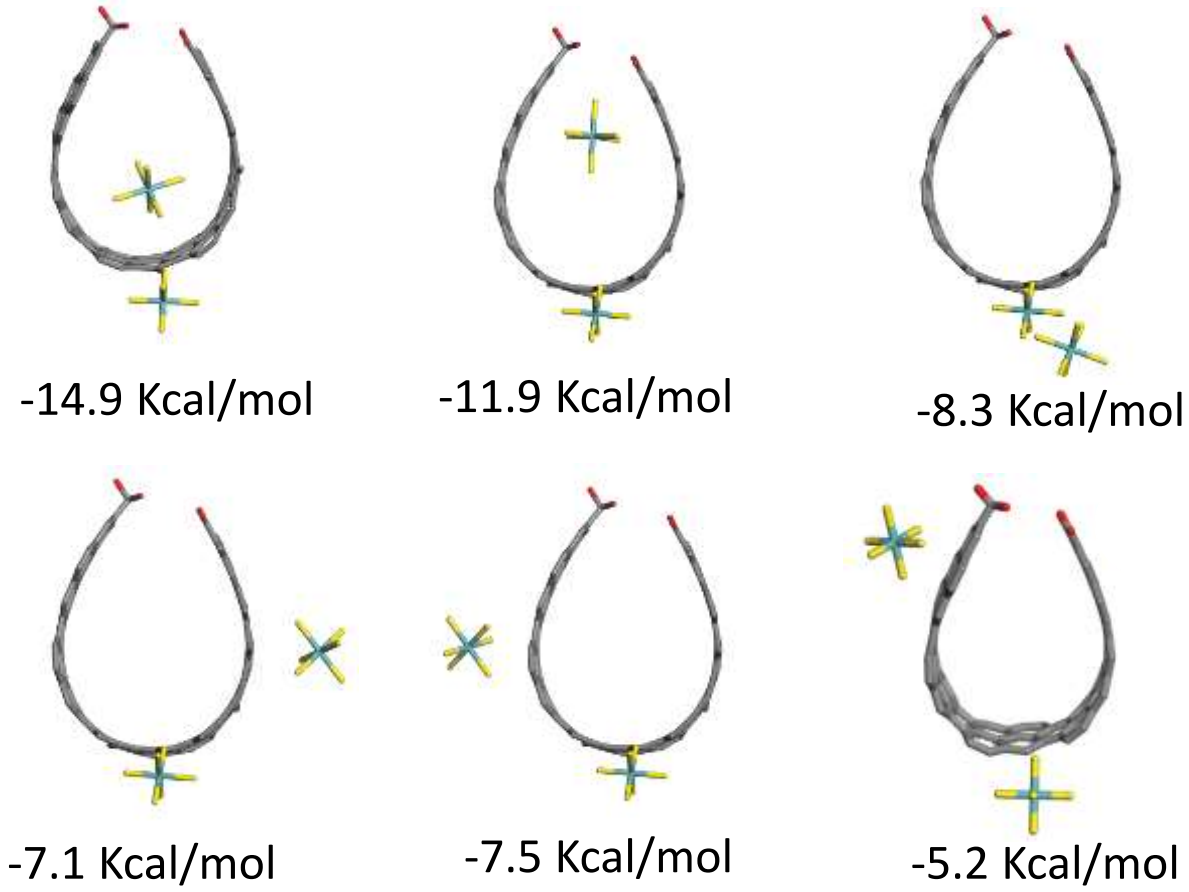

Fig. S17. Total energy of structures at different sites on C-GNR/ MoS_2.

3.1 Curvature induced lattice strain and dual active sites

It is known that the curvature induces a strain because of the lattice mismatch in CNTs due to bending. This strain energy increases quadratically with the bending angle. Unlike flat GNRs, the curvature in CNTS is partially preserved in C-GNRs and hence it also experiences the lattice strain. The curvature induced lattice strain leads to variation of electronic properties of graphene. Interestingly, when a curvature is introduced in the system, rehybridization of orbitals occur. The π orbitals are no more orthogonal to the surface, and instead are rehybridized due to the effect of the lower lying σ bonds due to the curvature-induced lattice strain. The curvature also enhances the spin orbit interaction and results in a variation of the spin orientation axis and an increase of the orbital angular momentum. The σ–π rehybridization effect can significantly change the band structures and resulting electronic distribution of resulting graphene systems[5-9].

The curvature-induced lattice strain in GNRs causes changes in electronic distribution and causes an increased electron density due to electron localization in the strained region. Our DFT analysis also confirmed the presence of high electron density hotspots near the center of the curvature (due to curvature-induced strain) and at the edges in C-GNRs (functional groups). In the F-GNRs, without curvature, high electron concentration sites are only available near the edges due to carboxylic acid functional groups. As the interaction between MoS_2 QDs and GNRs are vdW in nature (dipole-dipole), MoS_2 QDs can interact and anchor to the high electron density regions. As electron rich position in F-GNRs are only at the edges, it leads to GNR-MoS_2 active site to concentrate on the edges in F-GNRs. However, in C-GNRs, as high electron density is available at the edges and the curved center, MoS_2 QDs anchor on the edges and the center to result in two active sites. As the free energy of adsorption is different for the two positions, it leads to the catalytic wave, as seen in the case of C-GNR-MoS_2 heterostructures. The presence of such multiple catalytic active

sites leading to electrocatalytic wave for water-splitting reactions have been reported previously. In one of our previous works, we observed that MoS_2 C_{60} vdW heterostructures exhibit two well-defined catalytic waves for hydrogen evolution reaction. MoS_2/C_{60} system showed different fullerene arrangements, which were directly connected to the two catalytic HER waves.[10] Similar nature was also reported by Sanchez et al. The oxygen electroreduction of laccase−AuNPs displayed two electrocatalytic contributions, which were ascribed to the different electronic interactions between laccases and AuNPs.[11]

Catalyst	Onset potential (mV)	Reference
Nitrogen and Sulfur Co-Doped Nanoporous Graphene	**-130**	**12**
Graphitic Carbon Nitride Nanoribbons	**-80**	**13**
graphitic carbon nitride coupled with nanoporous graphene co-doped by S and Se	**-92**	**14**
cobalt phosphide embedded carbon matrix	**–77.74**	**15**
FeCo encapsulated Nitrogen doped Carbon nanotubes	**-70**	**16**
MoS_2-MoP nanosheet structures anchored on N-doped porous carbon	**-125**	**17**
This work	**-60**	

Table S2. Comparison of HER activities of various catalysts

Adsorption sites	E_{ads} **(eV)**	ΔG *free energy* **(eV)**
Pristine MoS_2 QD (S-active site)	0.23	0.2
F-GNR (skeletal C adjacent to -COOH group)	-0.152	-0.13
C-GNR (skeletal C near center of curvature)	-0.141	-0.12
F-GNR/MoS_2 (outer S atom)	-0.23	-0.19
F-GNR/MoS_2 (skeletal C adjacent to – COOH group)	-0.133	-0.14
F-GNR/MoS_2 (interfacial S atom)	-0.095	-0.09
C-GNR/MoS_2 (outer S atom)	-0.1265	-0.11
C-GNR.MoS_2 (skeletal C near center of curvature)	-0.150	-0.13
C-GNR/MoS_2 (interfacial S atom at the edge)	-0.1035	-0.08
C-GNR/MoS_2 (interfacial S atom at center of curvature)	-0.0575	-0.05

Table S3. Calculated Gibbs free energy (ΔG_H) for various sites for HER

References

1. D. V. Kosynkin, A. L. Higginbotham, A. Sinitskii, J. R. Lomeda, A. Dimiev, B. K. Price, and J. M. Tour., Nature 2009, **458**, 872-876

2. T. Wang, Z. Wang, R. V. Salvatierra, E. McHugh and J. M. Tour., Carbon 2020, **158**, 615-623

3. Mohanty, M. Ghorbani-Asl, S. Kretschmer, A. Ghosh, P. Guha, S. K. Panda, B. Jena, A. V. Krasheninnikov and B. K. Jena., ACS Catal. 2018, **8**, 1683-1689

4. M. F. Sanad, V. S. Chava, A. E. Shalan, L. G. Enriquez, T. Zheng, S. Pilla, and S. T. Sreenivasan., ACS Appl. Mater. Interfaces ,2021, **13**, 40731-40741

5. Chico, L., López-Sancho, M. P., & Muñoz, M. C., Phys. Rev. B, 2009, **79**, 235423.

6. Ding, J. W., Yan, X. H., Cao, J. X., Wang, D. L., Tang, Y., & Yang, Q. B., J. Phys. Condens. Matter, 2003, **15**, L439.

7. López-Sancho, M. P., & Munoz, M. C., Phys. Rev. B, 2011, **83**, 075406.

8. Kleiner, A., & Eggert, S.,Phys. Rev. B, 2001, **64**, 113402.

9. Shima, H.,Materials, 2011, **5**, 47-84.

10. Puente Santiago, A. R., He, T., Eraso, O., Ahsan, M. A., Nair, A. N., Chava, V. S., ... & Echegoyen, L., J. Am. Chem. Soc., 2020, **142**, 17923-17927.

11. Gutierrez-Sanchez, C., Pita, M., Vaz-Dominguez, C., Shleev, S., & De Lacey, A. L., J. Am. Chem. Soc., 2012, 134(41), 17212-17220.

12 Ito, Y.; Cong, W.; Fujita, T.; Tang, Z.; Chen, M., Angew. Chem., 2015, **127**, 2159-2164.

13 Zhao, Y.; Zhao, F.; Wang, X.; Xu, C.; Zhang, Z.; Shi, G.; Qu, L., Angew. Chem., Int. Ed., 2014, **53**, 13934-13939.

14 Shinde, S.; Sami, A.; Lee, J.-H., J. Mater. Chem. A.,2015, **3**, 12810-12819.

15 Li, M.; Liu, X.; Xiong, Y.; Bo, X.; Zhang, Y.; Han, C.; Guo, L., J. Mater. Chem. A., 2015, **3**, 4255-4265.

16. Deng, J.; Ren, P.; Deng, D.; Yu, L.; Yang, F.; Bao, X., Energy Environ. Sci., 2014, **7**, 1919-1923.

17. Yang, Y.; An, X.; Kang, M.; Guo, F.; Zhang, L.; Wang, Q.; Sun, D.; Liao, Y.; Yang, Z.; Lei, Z., New J. Chem., 2021, **45**, 14042-14049.